



OPEN

DATA DESCRIPTOR

Wide-field mosaics of the corneal subbasal nerve plexus in Parkinson's disease using in vivo confocal microscopy

Reza A. Badian¹✉, Stephan Allgeier², Fabio Scarpa³, Mattias Andréasson^{4,5,6}, Andreas Bartschat², Ralf Mikut², Alessia Colonna³, Marco Bellisario⁷, Tor Paaske Utheim^{8,9}, Bernd Köhler², Per Svenningsson^{4,5,6} & Neil Lagali^{7,9}✉

In vivo confocal microscopy (IVCM) is a non-invasive imaging technique facilitating real-time acquisition of images from the live cornea and its layers with high resolution (1–2 μm) and high magnification (600 to 800-fold). IVCM is extensively used to examine the cornea at a cellular level, including the subbasal nerve plexus (SBNP). IVCM of the cornea has thus gained intense interest for probing ophthalmic and systemic diseases affecting peripheral nerves. One of the main drawbacks, however, is the small field of view of IVCM, preventing an overview of SBNP architecture and necessitating subjective image sampling of small areas of the SBNP for analysis. Here, we provide a high-quality dataset of the corneal SBNP reconstructed by automated mosaicking, with an average mosaic image size corresponding to 48 individual IVCM fields of view. The mosaic dataset represents a group of 42 individuals with Parkinson's disease (PD) with and without concurrent restless leg syndrome. Additionally, mosaics from a control group ($n = 13$) without PD are also provided, along with clinical data for all included participants.

Background & Summary

Neurological disorders are a significant cause of disability and death worldwide. In the period from 1990 to 2015, the number of deaths from neurological disorders increased by 36.7%, with Parkinson's disease (PD) constituting the 12th most common condition leading to premature death (1.2%) among all neurological disorders in the overall global burden from neurological disorders in 2015¹.

PD is a progressive neurodegenerative disorder with its diagnosis based on clinical criteria consisting of a combination of bradykinesia with rigidity and/or rest tremor². Peripheral neuropathy (PN) that occurs in PD can exhibit both small and large fiber involvement^{3,4}. Additionally, restless legs syndrome (RLS), a sensorimotor condition, is frequently reported among patients suffering from neurological disorders including PD; therefore occurrence of RLS as comorbidity in PD patients has been the focus of multiple studies^{5–8}. As PN is difficult to diagnose, there has been much interest in the development and refinement of non-invasive examination modalities for its potential diagnosis. Increasingly, quantitative measures derived from non-invasive peripheral nerve imaging in the corneal subbasal nerve plexus are being reported as putative indicators of small fiber peripheral neuropathy in conditions such as diabetes mellitus^{9–17}. This technique is therefore of interest in the context of PD and RLS.

The cornea is a densely innervated tissue, whose sensory nerve bundles enter the cornea at the mid-stroma in a radial formation from the periphery^{18–21}. The stromal branches extend towards the central anterior cornea,

¹Unit of Regenerative Medicine, Department of Medical Biochemistry, Oslo University Hospital, Oslo, Norway.

²Institute for Automation and Applied Informatics, Karlsruhe Institute of Technology (KIT), Karlsruhe, Germany.

³Department of Information Engineering, University of Padua, Padua, Italy. ⁴Center for Neurology, Academic Specialist Center, Stockholm, Sweden. ⁵Department of Neurology, Karolinska University Hospital, Stockholm, Sweden.

⁶Department of Clinical Neuroscience, Karolinska Institutet, Stockholm, Sweden. ⁷Division of Ophthalmology, Institute for Biomedical and Clinical Sciences, Linköping University, Linköping, Sweden.

⁸Department of Ophthalmology, Oslo University Hospital, Oslo, Norway. ⁹Department of Ophthalmology, Sørlandet Hospital Arendal, Arendal, Norway. ✉e-mail: rezabadian@gmail.com; neil.lagali@liu.se

penetrate Bowman's layer, and then individual nerve fiber bundles separate and run parallel to the corneal surface, at the level of the corneal basal epithelium, forming the sub-basal nerve plexus (SBNP) supplying the sensory nerve fibers to the corneal epithelium^{18,20,22}. *In vivo* confocal microscopy (IVCM) is a clinical method of non-invasively examining the cornea, providing images with high lateral (1–2 μm) and axial (5–10 μm) resolution, at a magnification of up to 600²³ to 800 times²⁴. IVCM provides excellent images of the SBNP, from which parameters such as corneal nerve fiber length density (CNFL, measured as the sum of the nerve fiber length in mm divided by the corresponding SBNP area in mm^2), corneal nerve fiber number density (CNFD, the number of distinct nerve fibers (defined in various ways) per mm^2 of SBNP area), corneal nerve branch density (CNBD, the number of nerve branching points per mm^2 of SBNP area), and tortuosity (defined in various ways) can be measured^{10,16,18,20,25,26}. Only a few studies have used IVCM to examine corneal nerves in PD with some contradictory results. One study included 26 PD patients with varying disease duration and 26 controls. Using IVCM and selecting 4 to 6 single field-of-view images per eye for analysis, reduced CNFD, but increased CNBD and CNFL were found, compared to (healthy) controls²⁷. Another IVCM study, including 26 patients with early PD and 22 controls, analyzed 4 to 8 single field-of-view IVCM images of the SBNP per subject. The authors of the study reported that CNFL and CNBD were significantly reduced in PD patients compared to controls, while CNFD reduction was not statistically significant²⁸. Another study assessing 15 patients with moderate PD and 15 healthy controls, did not report the number of IVCM images analyzed per eye, but found a significant reduction in CNFL in PD patients relative to controls²⁹.

Here we present an IVCM dataset representing a larger number of patients ($n = 42$) compared to prior IVCM studies of PD. The raw data in this dataset was originally used³⁰ to investigate a possible relationship between the presence of RLS in PD and corneal nerve parameters. Here we provide an entire dataset of high quality wide-field mosaics of the corneal SBNP in PD patients (21 with and 21 without RLS) and 13 age-matched controls. We also provide the relevant clinical diagnostic information alongside the SBNP mosaics. The high quality wide-field mosaic images are a unique distinguishing feature in the present dataset, relative to prior IVCM studies. Our dataset represents the largest SBNP image sizes published to date, from any clinical cohort. The use of mosaics avoids the subjective selection of individual fields of view thus providing an objective view of the overall SBNP architecture, enabling accurate analysis of SBNP patterns and exact quantification of SBNP parameters^{16,31}. It has previously been shown that not using mosaics of the SBNP but using only small numbers of hand-selected images can lead to very large errors in the values of reported parameters³¹, possibly explaining wide discrepancies in previously reported values of SBNP in PD populations.

Moreover, inflammation is considered as one of the important etiological processes in PD as a neurodegenerative disease^{32–34}. The mosaic dataset provided here additionally contains inflammatory cell parameters that can be further analyzed for their relation to the various clinical disease parameters. To the best of our knowledge, no prior study in PD has investigated the inflammatory cells that are clearly visible at the level of the SBNP, although in other conditions these inflammatory cells (such as antigen-presenting dendritic cells) have been shown to be related to the onset of disease³⁵.

Methods

Study design, participants, inclusion and exclusion criteria. The initial study from which the raw IVCM data was collected³⁰ had a cross-sectional design, where participants were enrolled in the period from Spring 2018 to Autumn 2019 at the outpatient clinic at Center for Neurology and Karolinska University Hospital, Stockholm, Sweden. The study encompassed control participants without PD, and PD patients with (PD + RLS) and without RLS (PD-RLS) matched for age and sex. Participants were aged between 50 and 80 years and had to have one eye without history of previous corneal trauma, surgery or ongoing eye drop treatment. Patients fulfilled a diagnosis of clinically probable PD with or without RLS according to established criteria^{2,36}. PD + RLS ($n = 21$), PD – RLS ($n = 21$) and controls ($n = 13$) comprised the study. Written informed consent was obtained from all participants and the study was approved by the regional ethical board of Stockholm, Sweden (ref. nr 2018/264-31/2 (2019-03158)). Inclusion and exclusion criteria have been previously described in detail³⁰.

Clinical assessments. Details of the clinical, neurophysiological and biochemical assessments are outlined in our original study report³⁰. In short, demographic and disease-specific parameters were obtained by oral interview. Neurological rating scales included modified Hoehn and Yahr staging (mH&Y)^{37,38} and the Utah Early Neuropathy Scale (UENS)³⁹. The severity of RLS symptoms was evaluated with the International Restless Legs Scale rating scale (IRLS)⁴⁰ and the sensory suggested immobilization test was performed in the PD + RLS group^{41,42}. With regard to electrodiagnostic and quantitative sensory testing, details are described in the original study report³⁰.

***In Vivo* Confocal Microscopy Examination.** *In vivo* confocal microscopy of the cornea was performed to visualize the peripheral small fiber morphology of the corneal SBNP. IVCM image acquisition was conducted in both eyes of all participants, or in one eye in cases where the other eye did not meet the inclusion criteria. A single, experienced examiner performed all examinations using a Heidelberg Retinal Tomograph 3 with Rostock Corneal Module, HRT3-RCM (Heidelberg Engineering, Germany), using a built-in fixation light to bring the focus on to the central cornea. A motorized joystick module was used to control and maintain the focal plane at the desired corneal depth, at the SBNP level. The central and paracentral corneal regions were first imaged by translating the microscope field of view manually in a raster pattern, until regions were reached where the curvature of the cornea resulted in oblique images. Subsequently, to image the paracentral regions, the fixation light was moved sequentially in superior, inferior, temporal and nasal direction, with the manual raster scanning process being repeated for each fixation light position. During scanning, the depth of the SBNP was maintained

by manually adjusting the depth of focus by small movements on the joystick, in order to capture subtle variations in the plexus and enable a maximal projection of nerves to be made onto a 2D plane, as previously described³¹.

Differing from prior work, however, during the clinical examinations an attempt was made to image as large a wide-field area of the SBNP as possible by periodically pausing the examination to allow the subject and examiner to rest, then resuming the examination, until the examiner judged the imaged area to be of sufficient extent and quality, provided the subject was willing to cooperate with the strategy. The raw image datasets obtained from IVCN examination were then used as input to automated mosaic generation and nerve detection and quantification algorithms (described below).

Automated mosaic image generation. The process used to assemble SBNP mosaic images from the acquired datasets is identical to the method described in previous studies^{16,31}, with one notable exception described below. The mosaic generation process consisted of four consecutive process steps:

1. Removal of non-SBNP images from the dataset,
2. Pairwise, correlation-based image registration (using a decomposition of the images into 12 horizontal rectangular sub-images),
3. Formation and solution of a system of linear equations, yielding position coordinates of the sub-images, and
4. Construction of the mosaic image.

As it is not always possible to avoid the inclusion of non-SBNP images in the acquired datasets, these images were first removed from the processed data. The benefit of this is twofold. Non-SBNP images could negatively influence the contrast of the relevant SBNP image features if included in the mosaic algorithm, and removal of such images reduces mosaic-processing time if excluded early in the processing pipeline. Whereas the exclusion of non-SBNP images had been done manually in the past³¹, a tissue classification algorithm⁴³ was used in the initial PD³⁰ study to automatically identify and exclude non-SBNP images. The classifier is based on the Bag of Visual Words approach. It uses a trained feature extraction followed by a set of support vector machines, each of which had been trained to separate one characteristic corneal tissue class (epithelium, SBNP, stroma) from any other tissue class. A previous quantitative evaluation of the classifier reported a classification accuracy of over 96% on a manually labeled set of 663 IVCN images⁴³.

The image registration step makes use of the phase correlation function, a well-established approach for calculating the relative offset between two images⁴⁴. The phase correlation was calculated for all possible image pairs of a dataset to establish an estimation of the translational alignment between each image pair, but the key step in creating high-quality mosaic images is the decomposition of each image into 12 horizontal slices or sub-images and the calculation of the relative alignment d_{ij} (relating to the sub-images with indices i and j)^{31,45}. This approach was designed to analyze specifically the characteristic motion-induced image deformation artifacts that arise from the image formation process of the HRT-RCM microscope.

The third step of the mosaic generation process was the deduction of absolute, global position coordinates p_i for the sub-images from the translation vectors d_{ij} that had been calculated in the registration step. This global alignment process is based on the observation, that the translation vectors effectively estimate the position differences between respective sub-images, $d_{ij} = p_j - p_i$ ^{31,45}. After excluding all sub-image registration results with a correlation value below an empirically predefined threshold, these equations form a system of linear equations. The linear equation system always possesses degrees of freedom that need to be addressed by additional regularization terms: An additional equation $\lambda_1 p_0 = 0$ complements the otherwise purely difference equations with an absolute reference, and equations $\lambda_2(p_{i+1} - p_i) = 0$ (limited to pairs $(i, i + 1)$ of sub-images that belong to the same original image) provide alignment information for sub-images without any accepted registrations; λ_1 and λ_2 are weight factors. The regularized system of linear equations is subsequently solved for the sub-image position coordinates p_i .

The final mosaic image construction step was implemented as described previously³¹. Appropriate interpolation between the sub-image positions p_i yields position coordinates for single image rows, and the final mosaic image was then calculated by weighted averaging of overlapping original image data.

Optimizations of the mosaic image generation process. Runtime considerations were not a priority in the context of the present dataset. However, with regard to potential application in routine clinical practice (and also with regard to a larger number of patients in the future), the mosaic image generation process was reexamined with a particular focus on runtime optimization. The most effective means to reduce runtime is a size reduction of the images in the context of the image registration step, as the calculation time of the correlation function is dependent on the size of the input data. However, reducing the image information used for the correlation function inherently increases the noise level of the correlation function, making it harder to reliably separate correct registration results from incorrect ones. Scale factors of 3 and 2 for full image and sub-image correlations, respectively, have proven to be a good compromise.

Automated nerve tracing and nerve parameter quantification in SBNP mosaics. The algorithm used for automated nerve fiber tracing in mosaics was described earlier by Guimarães *et al.*⁴⁶. Briefly, this algorithm is based on three main steps: pre-processing, classification and post-processing. The pre-processing aims to improve the visibility of the corneal nerves. To achieve this goal, a Top-Hat morphological filtering was used to equalize the background and to improve the contrast of the image. A bank of log-Gabor filters, each with a different orientation, highlights linear structures and completes the pre-processing. A threshold was then applied

Parameter	Description
Subject ID	Identification number assigned to each of the subjects in the study cohort (1 to 57)
Image name	File name assigned to each image in the wide-field mosaics dataset
Eye	Image and clinical data corresponding to right eye (RE) or left eye (LE)
Mosaic area	Area of the corneal subbasal nerve plexus represented in the mosaic image (mm ²). In all cases, regions without image data (black or empty areas) were not included in the area calculation.
mCNFL	Mosaic corneal nerve fiber length density: the total length of all nerves in the mosaic divided by the mosaic area expressed in (mm/mm ²)
mCNBD	Mosaic corneal nerve branch density; defined as total number of branching points divided by the mosaic area and expressed as the number of branching points per mm ² (nr./mm ²)
wCNFL	Whorl corneal nerve fiber length density; defined as corneal subbasal nerve fiber length density in the whorl region (in mm/mm ²), based on automated nerve tracing. wCNFL is provided for 800 μm and 400 μm diameter whorl regions in full and half-circle areas (see Fig. 3). Only values for eyes where the full circle contained image data are included.
wCNBD	Whorl corneal nerve branch density defined as total number of branching points in the whorl region divided by the mosaic area expressed as the number of branching points per mm ² . wCNBD is provided for the four different definitions of the whorl as for wCNFL.
mDCs	Density of mature dendritic cells in each mosaic, in cells/mm ² of mosaic area.
imDCs	Density of immature dendritic cells in each mosaic, in cells/mm ² of mosaic area.
GCs	Density of globular cells in each mosaic, in cells/mm ² of mosaic area.

Table 1. Study parameters related to the IVCN data obtained and provided in the mosaic dataset.

Parameter	Description
Subject ID	Identification number of the subject in the cohort (57 subjects of which 2 were excluded).
Study Group	Controls, PD + RLS, or PD – RLS
Age	Subject age at time of study inclusion (years)
Sex	1 = Male, 0 = Female
Smoking	Smoking status, 1 = yes, 0 = no
Coffee intake	Consumption of coffee (cups/day)
Intake of B12 supplements or multivitamins	1 = yes, 0 = no
PD motor duration	Duration of motor symptoms (years)
RLS duration	Duration of restless legs syndrome (years)
L-dopa duration	Duration of treatment with L-dopa (years)
LEDD	L-dopa equivalent daily dose (mg)
Ongoing L-dopa therapy	1 = yes, 0 = no
mH&Y (stage)	Modified Hoehn and Yahr scale for staging Parkinson's symptoms and disability
IRLS	International RLS study group rating scale (IRLS): 0–40
UENS	Utah Early Neuropathy Scale. Clinical rating scale for the assessment of peripheral neuropathy.
p-homocysteine	Concentration of homocysteine in plasma (μmol/L)
s-methylmalonic acid	Concentration of methylmalonic acid in serum (μmol/L)
p-pyridoxal-5'-phosphate	Concentration of pyridoxal-5'-phosphate in plasma (nmol/L)
s-ferritin	Concentration of ferritin in serum (μg/L)

Table 2. List of clinical and demographic parameters linked to each study subject in the provided data set. Blood parameters were based on fasting whole blood samples acquired using venipuncture. L-dopa: Levodopa.

to identify pixels corresponding to a nerve. From the selected pixels, morphological and intensity-based features are extracted and used as input for a finer classification based on the support vector machines approach. The final classification consists in a label “nerve” or “other” assigned to each pixel of the image. A binary image was then obtained, in which white pixels correspond to nerves and black pixels correspond to the other.

The resulting binary image contains nerve segments with small gaps between each other, due to noise in the original image. Thus, to improve the nerve tracing, the post-processing step performs morphological operations and traces missing connections⁴⁷. In addition, the algorithm computes all possible connection-paths between segments based on distance, angle, and intensity. The best connection-path is then chosen based on the Dijkstra algorithm⁴⁸.

From the automated nerve tracing, quantitative nerve parameters were extracted. For the current mosaic dataset, the algorithm provided the mosaic corneal nerve fiber length density (mCNFL), defined as the total length of all nerves in the mosaic divided by the mosaic area (black regions excluded) expressed in mm/mm², and the mosaic corneal nerve branching density (mCNBD) defined as the total number of branching points divided by the mosaic area (black region excluded) expressed as the number of branching points per mm².

The inferocentral whorl region of the subbasal plexus normally contains the highest concentration of subbasal nerves, and this region has been analyzed separately in several studies^{31,49–51}. Here, subbasal nerve parameters

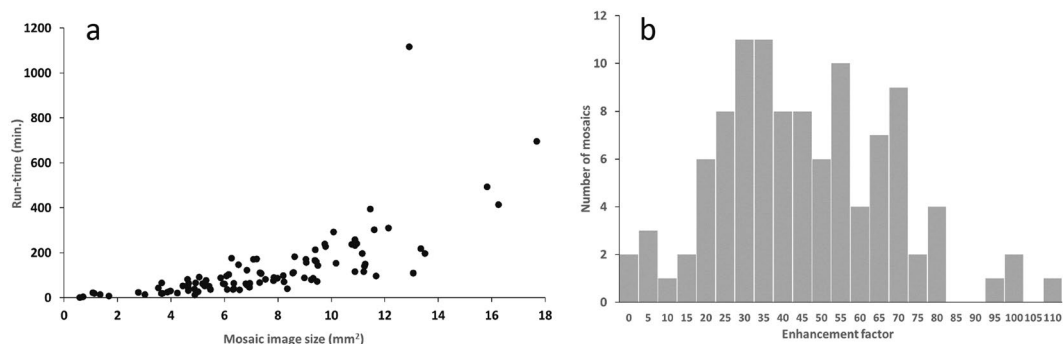


Fig. 1 Characterization of mosaic computation and size. **(a)** Scatter plot for run-times for mosaic image generation in relation to mosaic image size. **(b)** Histogram of distribution of number of mosaics for each enhancement factor (enhancement factor is mosaic area divided by the area of a single $400 \times 400 \mu\text{m}$ IVCM frame).

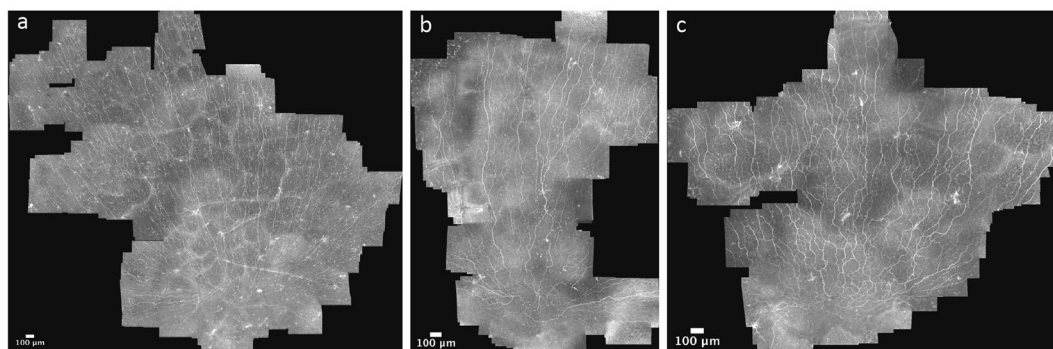


Fig. 2 Representative IVCM mosaic images of the corneal subbasal nerve plexus for the three study groups. **(a)** Control. **(b)** Subject with PD with RLS. **(c)** Subject with PD without RLS.

in the whorl region were analyzed by the automated tracing algorithm described above. Whorl corneal nerve fiber length (wCNFL) and whorl corneal nerve branch density (wCNBD) in the whorl region were automatically calculated from automated tracing with respect to four configurations; for nerves within a full circular region centered on the whorl center with either an $800 \mu\text{m}$ diameter or $400 \mu\text{m}$ diameter, and for the corresponding superior semi-circular regions (extending from 9 to 3 o'clock) only. Nerve analyses were performed across control, PD – RLS and PD + RLS groups, and again for controls vs. all PD participants.

Inflammatory cell analysis within the SBNP. Additionally, it is possible to analyze the mosaic dataset for the presence of inflammatory cells/dendritic cells (DCs), and with respect to the different DC subtypes whose morphologic features have been described in an earlier study³⁵. Here, two independent experienced observers performed morphological characterization and quantification of the inflammatory DCs present in the SBNP. The two observers were masked to the identity of each mosaic image. Three types of DCs were quantified: mature DCs, immature DCs and globular cells³⁵. The DC density values, expressed as cells per mm² of mosaic area for the various subtypes, were averaged across observers and across both eyes for all participants. This data is also provided along with the mosaic dataset.

Statistical analysis. Statistical analyses of presented data were performed using IBM SPSS statistics for Windows, version 25.0 (IBM Corp., Armonk, N.Y., USA). A two-tailed P value of < 0.05 was considered significant.

Data Records

Data for the wide field mosaic images of the corneal subbasal plexus that were acquired for PD patients and control participants are provided⁵². The Excel file contains the numeric data and the corresponding mosaic image numbers, and is therefore the ‘key’ to the mosaic image dataset. IVCM mosaic images represent the largest mosaic per eye and are provided in TIFF format, labeled with the subject ID number (01 to 57 – two participants were excluded hence non-consecutive numbering) and the eye (RE for right eye and LE for left eye). Table 1 details the parameters associated with the SBNP mosaic dataset. In addition, we provide in the same file the clinical parameters linked to each study subject (Table 2). Finally, we provide folders for each eye (in ZIP format) containing the raw, non-stitched IVCM images used to create each corresponding mosaic image.

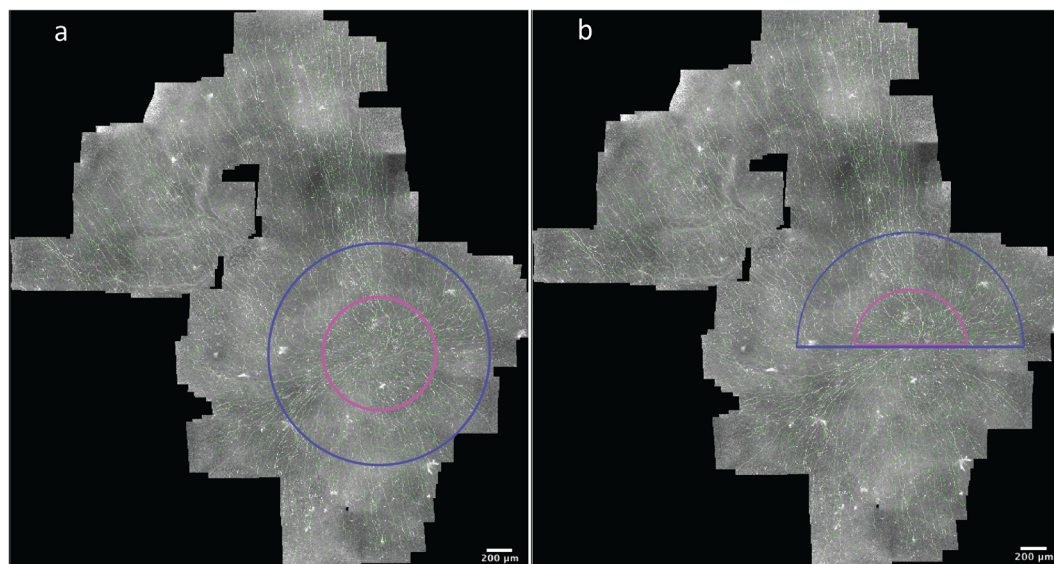


Fig. 3 Mosaic image illustrating regions analyzed for inferocentral whorl parameter wCNFL. (a) Mosaic image depicting region of 800 μm radius (blue) and 400 μm radius (magenta) centered on the whorl center. (b) Mosaic image depicting upper half circle of 800 μm radius (blue) and 400 μm radius (magenta) based on the whorl center.

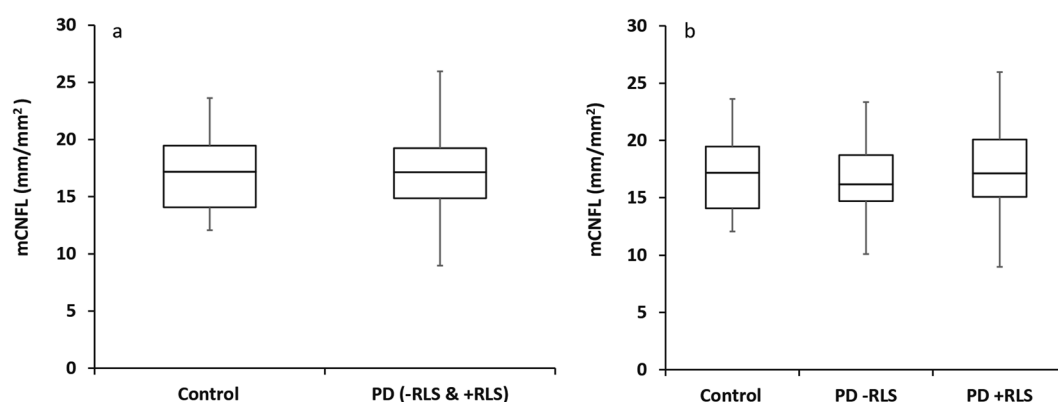


Fig. 4 Box plots comparing mCNFL among the study groups. (a) Box plot comparing healthy controls vs. all Parkinson's disease (PD) patients as a single group, t-test $P = 0.62$. (b) Box plot comparing all study subgroups including PD patients with and without RLS, ANOVA $P = 0.79$. Data represents quantification based on the single largest mosaic per eye, differing slightly from prior analyses where in some cases average values from several mosaics per eye were used³⁰.

Technical Validation

The average (mean \pm standard deviation) percentage of SNP-classified images from a given eye was $59.2 \pm 15.8\%$. The overall runtime of the mosaic image generation process is dominated by the image registration step, which exhibits a quadratic runtime behavior with respect to the SBNP-filtered dataset size when registering all possible image pairs. The following overall runtimes are therefore not normally distributed and are given as median (interquartile range). The overall runtime measured in the study process pipeline (i.e. not applying the runtime optimizations), was 88.6 (45.8, 166.1) minutes per eye (Fig. 1a). After employing the runtime optimizations, particularly including scaling down the images prior to phase correlation, the runtime of the entire process decreased to 3.0 (1.6, 5.7) minutes per eye. The resulting mosaic image quality was comparable with both approaches, as examined by visual comparison. Figure 1 shows a scatter plot of the runtime for mosaic generation in relation to the size of respective mosaic images in the study cohort, and to the number of individual raw IVCN images used to generate each corresponding mosaic. Runtimes are based on a Windows PC system (Core2 Duo, E8400, 2×3 GHz, 6GB RAM).

The average (mean \pm standard deviation) mosaic size per eye was 7.69 ± 3.53 mm² across a total of 106 mosaics, for the original process used for study evaluation. This corresponds to a mean enhancement factor of 48 across all 106 mosaics, meaning an equivalent mean tiled area of 48 individual IVCN image frames. Figure 1b shows the distribution of the number of mosaics with corresponding enhancement factor in the present dataset.

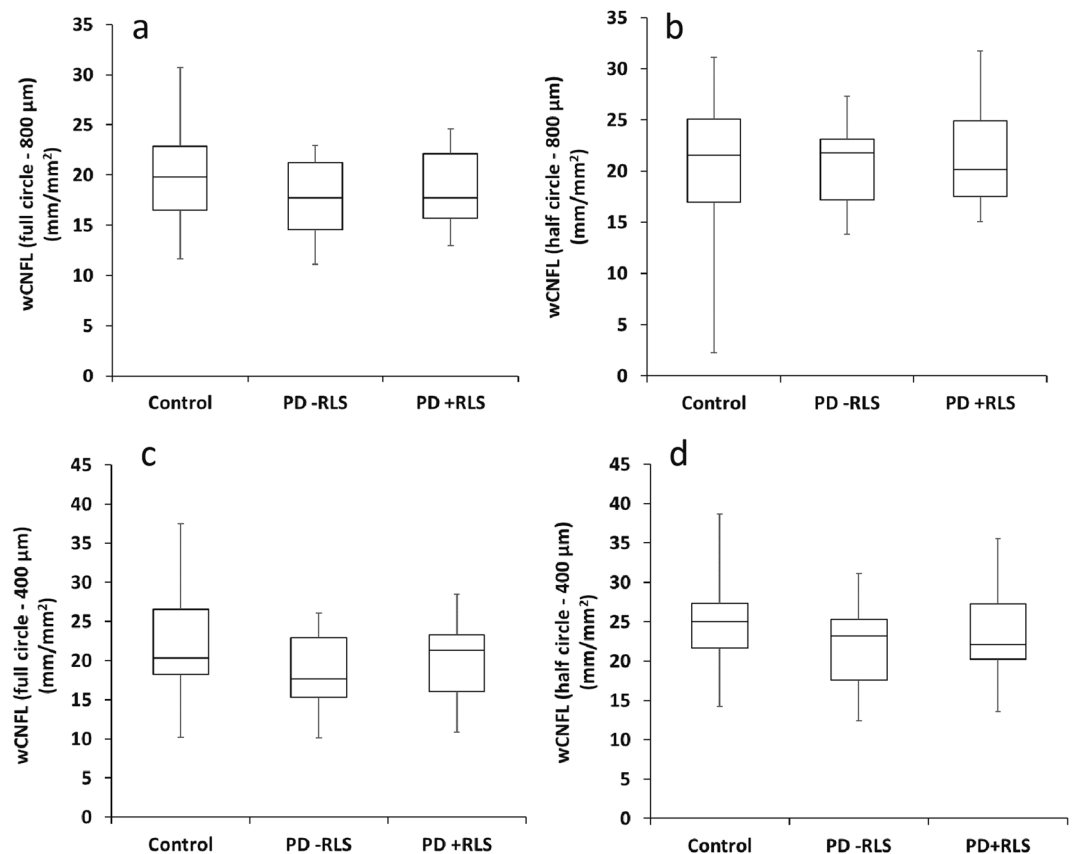


Fig. 5 Box plots indicating comparisons of wCNFL across study groups. **(a,b)** Comparison of wCNFL across the three study groups. **(a)** Full circular whorl region of 800 μm diameter, ANOVA $P = 0.47$. **(b)** Half-circle region of 800 μm diameter, ANOVA $P = 0.77$. **(c,d)** The corresponding box plots for the whorl defined in a 400 μm diameter region. **(c)** Full circular whorl region of 400 μm diameter, ANOVA $P = 0.36$. **(d)** Half-circle region of 400 μm diameter, ANOVA $P = 0.47$.

	Inflammatory cell type		
	mDCs	imDCs	GCs
Mean difference	9.3	-4.9	-0.8
SD	12.7	30.0	2.6
Lower 95% LOA	-15.6	-63.8	-5.9
Upper 95% LOA	34.3	54.0	4.3
Pearson's r	0.68	0.74	0.98

Table 3. Overview of inter-observer differences in dendritic cell quantification from mosaic images. Values represent the mean difference between the two observers, standard deviation of difference and lower and upper bounds of the 95% limits of agreement (LOA) for dendritic cell density in cells/ mm^2 of mosaic area, for each given cell type. Identification and quantification of inflammatory cells was based on three cell types: mDCs: Mature dendritic cells, imDCs: immature dendritic cells, and GCs: globular cells. The correlation coefficient between observers (Pearson's r) is shown for each cell type.

The data presented here represents the mosaic with the largest size for each eye, differing slightly from prior analyses where in some cases average values from several mosaics per eye were used³⁰. It is interesting to note that using the runtime-optimized algorithms, the average size of the largest mosaic image for a given eye decreased to $7.15 \pm 3.30 \text{ mm}^2$, with either no area reduction or an area reduction of less than 5% of the original mosaic image area in 69% of the mosaics. It is worth noting that – for both the optimized and the non-optimized process alike – the original images that could not be integrated into the single largest mosaic image per eye are still assembled into separate, smaller mosaic images. Figure 2(a–c) shows representative SBNP mosaics from the control, PD + RLS and PD – RLS groups.

Figure 3(a,b) depicts examples of the automatically traced mosaics. The traced nerves and identified branching points were quantified with respect to the entire mosaic image area, as well as the plexus area limited to the

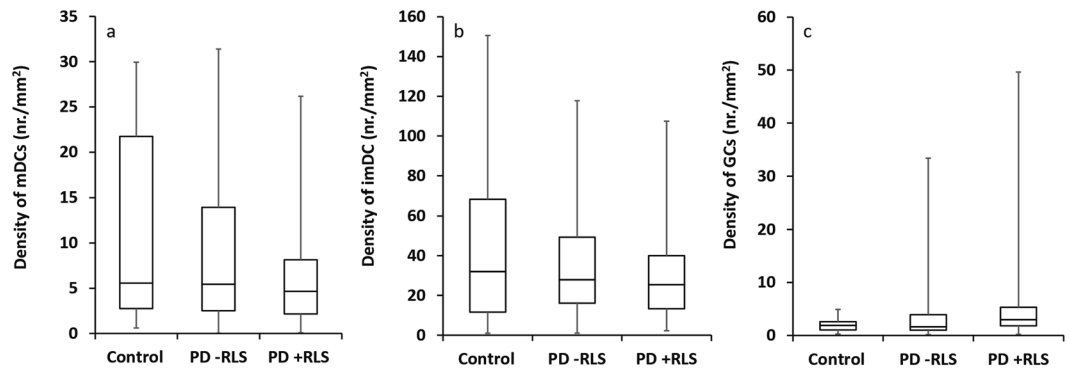


Fig. 6 Box plots indicating comparisons for inflammatory cells across study groups. **(a)** Density of mature dendritic cells (mDCs), ANOVA $P = 0.58$. **(b)** Density of immature dendritic cells (imDCs), ANOVA $P = 0.54$. **(c)** Density of globular cells (GCs), ANOVA $P = 0.19$.

indicated whorl regions. We provide the nerve parameter data for these analyses as part of the current dataset. Example comparisons of mCNFL and wCNFL across the various groups are given in Fig. 4(a,b) and Fig. 5(a–d).

The validity of the manual inflammatory cell quantification in mosaics by the two observers was determined by the Bland-Altman analysis method of inter-observer agreement⁵³. The mean, standard deviation (SD) and the 95% limits of agreement (LOA) between observers for the difference in cell density for each cell type across all mosaics is presented in Table 3, along with the correlation between observers measured by Pearson's r . As an example of the inflammatory cell data, the density of mature and immature dendritic cells (mDCs, imDCs, respectively), and globular cells (GCs) are plotted across the three subject groups (Fig. 6a–c).

Code availability

Computational codes used to, firstly, perform the depth-corrected mosaics synthesis used in the study and, secondly, for automated nerve tracing were developed by the academic institutions of Karlsruhe Institute of Technology and University of Padua, respectively, and are exclusively intended for scientific research use^{30,31}. The developers of the respective algorithms are willing to apply the code to user-supplied raw IVCM data in the form of academic collaborations. Interested parties are requested to contact the respective researchers for mosaic creation (Allgeier) and automated nerve analyses (Scarpa).

Received: 7 May 2021; Accepted: 28 October 2021;

Published online: 26 November 2021

References

- Feigin, V. L. *et al.* Global, regional, and national burden of neurological disorders during 1990–2015: a systematic analysis for the Global Burden of Disease Study 2015. *The Lancet. Neurology* **16**, 877–897 (2017).
- Postuma, R. B. *et al.* MDS clinical diagnostic criteria for Parkinson's disease. *Mov Disord* **30**, 1591–1601 (2015).
- Toth, C. *et al.* Levodopa, methylmalonic acid, and neuropathy in idiopathic Parkinson disease. *Annals of neurology* **68**, 28–36 (2010).
- Doppler, K. *et al.* Cutaneous neuropathy in Parkinson's disease: a window into brain pathology. *Acta neuropathologica* **128**, 99–109 (2014).
- Gómez-Esteban, J. C. *et al.* Restless legs syndrome in Parkinson's disease. *Movement disorders: official journal of the Movement Disorder Society* **22**, 1912–1916 (2007).
- Möller, J. C., Unger, M., Stiasny-Kolster, K. & Oertel, W. H. Restless Legs Syndrome (RLS) and Parkinson's disease (PD)-related disorders or different entities? *Journal of the neurological sciences* **289**, 135–137 (2010).
- Angelini, M., Negrotti, A., Marchesi, E., Bonavina, G. & Calzetti, S. A study of the prevalence of restless legs syndrome in previously untreated Parkinson's disease patients: absence of co-morbid association. *Journal of the neurological sciences* **310**, 286–288 (2011).
- Rijsman, R. M., Schoolderman, L. F., Rundervoort, R. S. & Louter, M. Restless legs syndrome in Parkinson's disease. *Parkinsonism & related disorders* **20**(Suppl 1), S5–9 (2014).
- Malik, R. A. *et al.* Corneal confocal microscopy: a non-invasive surrogate of nerve fibre damage and repair in diabetic patients. *Diabetologia* **46**, 683–688 (2003).
- Messmer, E. M., Schmid-Tannwald, C., Zapp, D. & Kampik, A. *In vivo* confocal microscopy of corneal small fiber damage in diabetes mellitus. *Graefes' archive for clinical and experimental ophthalmology = Albrecht von Graefes Archiv fur klinische und experimentelle Ophthalmologie* **248**, 1307–1312 (2010).
- Perkins, B. A. *et al.* Corneal confocal microscopy for identification of diabetic sensorimotor polyneuropathy: a pooled multinational consortium study. *Diabetologia* **61**, 1856–1861 (2018).
- Jiang, M. S., Yuan, Y., Gu, Z. X. & Zhuang, S. L. Corneal confocal microscopy for assessment of diabetic peripheral neuropathy: a meta-analysis. *The British journal of ophthalmology* **100**, 9–14 (2016).
- Tavakoli, M. *et al.* Corneal confocal microscopy: a novel noninvasive test to diagnose and stratify the severity of human diabetic neuropathy. *Diabetes care* **33**, 1792–1797 (2010).
- Petropoulos, I. N. *et al.* Corneal nerve loss detected with corneal confocal microscopy is symmetrical and related to the severity of diabetic polyneuropathy. *Diabetes Care* **36**, 3646–3651 (2013).
- Petropoulos, I. N. *et al.* Rapid automated diagnosis of diabetic peripheral neuropathy with *in vivo* corneal confocal microscopy. *Investigative ophthalmology & visual science* **55**, 2071–2078 (2014).
- Lagali, N. S. *et al.* Reduced Corneal Nerve Fiber Density in Type 2 Diabetes by Wide-Area Mosaic Analysis. *Invest Ophthalmol Vis Sci* **58**, 6318–6327 (2017).

17. Ferdousi, M. *et al.* Diabetic Neuropathy Is Characterized by Progressive Corneal Nerve Fiber Loss in the Central and Inferior Whorl Regions. *Investigative ophthalmology & visual science* **61**, 48 (2020).
18. Muller, L. J., Pels, L. & Vrensen, G. F. Ultrastructural organization of human corneal nerves. *Investigative ophthalmology & visual science* **37**, 476–488 (1996).
19. Oliveira-Soto, L. & Efron, N. Morphology of corneal nerves using confocal microscopy. *Cornea* **20**, 374–384 (2001).
20. Müller, L. J., Marfurt, C. F., Kruse, F. & Tervo, T. M. Corneal nerves: structure, contents and function. *Exp. Eye Res.* **76**, 521–542 (2003).
21. Eghrari, A. O., Riazuddin, S. A. & Gottsch, J. D. Overview of the Cornea: Structure, Function, and Development. *Progress in molecular biology and translational science* **134**, 7–23 (2015).
22. Oliveira-Soto, L. & Efron, N. Morphology of corneal nerves in soft contact lens wear. A comparative study using confocal microscopy. *Ophthalmic & physiological optics: the journal of the British College of Ophthalmic Opticians (Optometrists)* **23**, 163–174 (2003).
23. Jalbert, I., Stapleton, F., Pappas, E., Sweeney, D. F. & Coroneo, M. *In vivo* confocal microscopy of the human cornea. *The British journal of ophthalmology* **87**, 225–236 (2003).
24. Stachs, O., Guthoff, R. F. & Aumann, S. *In Vivo Confocal Scanning Laser Microscopy*. in *High Resolution Imaging in Microscopy and Ophthalmology: New Frontiers in Biomedical Optics* (ed. Bille, J. F.) 263–284 (Springer International Publishing, Cham, 2019).
25. Tavakoli, M., Petropoulos, I. N. & Malik, R. A. Corneal confocal microscopy to assess diabetic neuropathy: an eye on the foot. *Journal of diabetes science and technology* **7**, 1179–1189 (2013).
26. Lagali, N. *et al.* Focused Tortuosity Definitions Based on Expert Clinical Assessment of Corneal Subbasal Nerves. *Investigative ophthalmology & visual science* **56**, 5102–5109 (2015).
27. Kass-Iliyya, L. *et al.* Small fiber neuropathy in Parkinson's disease: A clinical, pathological and corneal confocal microscopy study. *Parkinsonism & related disorders* **21**, 1454–1460 (2015).
28. Podgorny, P. J., Suchowersky, O., Romanchuk, K. G. & Feasby, T. E. Evidence for small fiber neuropathy in early Parkinson's disease. *Parkinsonism & related disorders* **28**, 94–99 (2016).
29. Misra, S. L., Kersten, H. M., Roxburgh, R. H., Danesh-Meyer, H. V. & McGhee, C. N. Corneal nerve microstructure in Parkinson's disease. *Journal of clinical neuroscience: official journal of the Neurosurgical Society of Australasia* **39**, 53–58 (2017).
30. Andréasson, M. *et al.* Parkinson's disease with restless legs syndrome—an *in vivo* corneal confocal microscopy study. *NPJ Parkinsons Dis* **7**, 4 (2021).
31. Lagali, N. S. *et al.* Wide-field corneal subbasal nerve plexus mosaics in age-controlled healthy and type 2 diabetes populations. *Sci Data* **5**, 180075 (2018).
32. Whitton, P. S. Inflammation as a causative factor in the aetiology of Parkinson's disease. *British journal of pharmacology* **150**, 963–976 (2007).
33. Tansey, M. G. & Goldberg, M. S. Neuroinflammation in Parkinson's disease: its role in neuronal death and implications for therapeutic intervention. *Neurobiology of disease* **37**, 510–518 (2010).
34. De Lella Ezcurra, A. L., Chertoff, M., Ferrari, C., Graciarena, M. & Pitossi, F. Chronic expression of low levels of tumor necrosis factor-alpha in the substantia nigra elicits progressive neurodegeneration, delayed motor symptoms and microglia/macrophage activation. *Neurobiology of disease* **37**, 630–640 (2010).
35. Lagali, N. S. *et al.* Dendritic cell maturation in the corneal epithelium with onset of type 2 diabetes is associated with tumor necrosis factor receptor superfamily member 9. *Sci Rep* **8**, 14248 (2018).
36. Allen, R. P. *et al.* Restless legs syndrome/Willis-Ekbom disease diagnostic criteria: updated International Restless Legs Syndrome Study Group (IRLSSG) consensus criteria—history, rationale, description, and significance. *Sleep Med* **15**, 860–873 (2014).
37. Goetz, C. G. *et al.* Movement Disorder Society Task Force report on the Hoehn and Yahr staging scale: status and recommendations. *Mov Disord* **19**, 1020–1028 (2004).
38. Hoehn, M. M. & Yahr, M. D. Parkinsonism: onset, progression and mortality. *Neurology* **17**, 427–442 (1967).
39. Singleton, J. R. *et al.* The Utah Early Neuropathy Scale: a sensitive clinical scale for early sensory predominant neuropathy. *J Peripher Nerv Syst* **13**, 218–227 (2008).
40. Walters, A. S. *et al.* Validation of the International Restless Legs Syndrome Study Group rating scale for restless legs syndrome. *Sleep Med* **4**, 121–132 (2003).
41. De Cock, V. C. *et al.* Suggested immobilization test for diagnosis of restless legs syndrome in Parkinson's disease. *Movement disorders: official journal of the Movement Disorder Society* **27**, 743–749 (2012).
42. Michaud, M., Lavigne, G., Desautels, A., Poirier, G. & Montplaisir, J. Effects of immobility on sensory and motor symptoms of restless legs syndrome. *Movement disorders: official journal of the Movement Disorder Society* **17**, 112–115 (2002).
43. Bartschat, A. *et al.* Fuzzy tissue detection for real-time focal control in corneal confocal microscopy. *at - Automatisierungstechnik* **67**, 879–888 (2019).
44. Foroosh, H., Zerubia, J. B. & Berthod, M. Extension of phase correlation to subpixel registration. *IEEE transactions on image processing: a publication of the IEEE Signal Processing Society* **11**, 188–200 (2002).
45. Allgeier, S. *et al.* Elastische Registrierung von *in-vivo*-CLSM-Aufnahmen der Kornea. in *Bildverarbeitung für die Medizin 2011: Algorithmen - Systeme - Anwendungen Proceedings des Workshops vom 20-22 März 2011 in Lübeck* (eds. Handels, H., Ehrhardt, J., Deserno, T. M., Meinzer, H.-P. & Tolxdorff, T.) 149–153 (Springer Berlin Heidelberg, Berlin, Heidelberg, 2011).
46. Guimaraes, P., Wigdahl, J. & Ruggeri, A. A Fast and Efficient Technique for the Automatic Tracing of Corneal Nerves in Confocal Microscopy. *Transl Vis Sci Technol* **5**, 7 (2016).
47. Scarpa, F., Grisan, E. & Ruggeri, A. Automatic recognition of corneal nerve structures in images from confocal microscopy. *Investigative ophthalmology & visual science* **49**, 4801–4807 (2008).
48. Dijkstra, E. W. A note on two problems in connexion with graphs. *Numerische Mathematik* **1**, 269–271 (1959).
49. Patel, D. V. & McGhee, C. N. Mapping of the normal human corneal sub-Basal nerve plexus by *in vivo* laser scanning confocal microscopy. *Invest. Ophthalmol. Vis. Sci.* **46**, 4485–4488 (2005).
50. Utsunomiya, T. *et al.* Imaging of the Corneal Subbasal Whorl-like Nerve Plexus: More Accurate Depiction of the Extent of Corneal Nerve Damage in Patients With Diabetes. *Invest. Ophthalmol. Vis. Sci.* **56**, 5417–5423 (2015).
51. Pritchard, N. *et al.* Utility of Assessing Nerve Morphology in Central Cornea Versus Whorl Area for Diagnosing Diabetic Peripheral Neuropathy. *Cornea* **34**, 756–761 (2015).
52. Badian, R. A. *et al.* Wide-field mosaic dataset of the corneal subbasal nerve plexus in Parkinson's disease using *in vivo* confocal microscopy. [figshare https://doi.org/10.6084/m6089.figshare.14481249](https://doi.org/10.6084/m6089.figshare.14481249) (2021).
53. Bland, J. M. & Altman, D. G. Statistical methods for assessing agreement between two methods of clinical measurement. *Lancet (London, England)* **1**, 307–310 (1986).

Acknowledgements

Authors wish to acknowledge the kind assistance and support of the outpatient clinic at Center for Neurology and Karolinska University Hospital, Stockholm where study participants were recruited to the original study that was approved by the regional ethical board of Stockholm, Sweden (ref. nr 2018/264-31/2 (2019-03158)). The study was funded by Hofgren's fond, NEURO Sweden. Parts of this work were funded by the Deutsche Forschungsgemeinschaft (DFG, German Research Foundation; project nr. 273371152).

Author contributions

R.A.B. designed and conducted evaluations of the subbasal nerve plexus related parameters, analyzed data for validation purposes, and wrote the manuscript. N.L. designed and conceived the original IVCM study, performed IVCM examinations, analyzed data for validation purposes, interpreted data, and contributed to writing the manuscript. S.A., B.K., A.B. and R.M. conceived, developed, tested and optimized mosaic image generation algorithms, provided the mosaics, and contributed to writing the manuscript. F.S. and A.C. developed and customized the algorithm for the automated nerve fiber tracing, performed automated nerve parameter analysis and data extraction from whole and partial mosaics, and contributed to writing the manuscript. M.B. analyzed mosaics and manually quantified inflammatory cells. M.A. conceived and designed the original clinical study, designed and conducted the Parkinson's disease-specific neurological examinations, and obtained all clinical parameter data. P.S. conceived and designed the original clinical study, and designed, evaluated, and interpreted the Parkinson's disease specific neurological examinations. T.P.U. contributed to study coordination, implementation and drafting the manuscript. All authors critically reviewed and revised the manuscript.

Competing interests

The authors declare no competing interests.

Additional information

Correspondence and requests for materials should be addressed to R.A.B. or N.L.

Reprints and permissions information is available at www.nature.com/reprints.

Publisher's note Springer Nature remains neutral with regard to jurisdictional claims in published maps and institutional affiliations.



Open Access This article is licensed under a Creative Commons Attribution 4.0 International License, which permits use, sharing, adaptation, distribution and reproduction in any medium or format, as long as you give appropriate credit to the original author(s) and the source, provide a link to the Creative Commons license, and indicate if changes were made. The images or other third party material in this article are included in the article's Creative Commons license, unless indicated otherwise in a credit line to the material. If material is not included in the article's Creative Commons license and your intended use is not permitted by statutory regulation or exceeds the permitted use, you will need to obtain permission directly from the copyright holder. To view a copy of this license, visit <http://creativecommons.org/licenses/by/4.0/>.

The Creative Commons Public Domain Dedication waiver <http://creativecommons.org/publicdomain/zero/1.0/> applies to the metadata files associated with this article.

© The Author(s) 2021